Image-Reversal Soft Lithography: Fabrication of Ultrasensitive Biomolecular Detectors

Tina Saberi Safaei, Jagotamoy Das, Sahar Sadat Mahshid, Peter M. Aldridge, Edward H. Sargent,* and Shana O. Kelley*

Integrated circuits for the analysis of biomolecules have the potential to enable rapid and convenient point-of-care (POC) diagnostics.[1] Spectroscopic,[2] electronic,[3] and mechanical[4] sensing strategies have allowed rapid advances in POC detection, as have electrochemical biosensors.[1b] The applicability of the electrochemical systems has been demonstrated in the detection of analytes in biological samples ranging from cancer cells[5] to nucleic acids and proteins.[6]

It has been shown that high sensitivities can be achieved in the case of electrochemical detectors by enhancing the efficiency with which analyte molecules bind specifically to molecular probes displayed on the biosensor surface. The use of nanometer-sized electrodes, while advantageous for the display of probe molecules on their nanoscale-curved surfaces, comes at the expense of speed of detection.[7] Diffusive mass transport of analyte molecules to individual nanoscale sensors is limited to the point that the detection of analyte molecules at lower than picomolar concentrations is not feasible within practical time scales.

Fortunately, it has recently been proven that macroscopically sized (microns and larger) electrodes, particularly those that have been finely nanostructured, can overcome the limitations of diffusive transport impeding the performance of nanosized sensors. These nanostructured microelectrodes (NMEs) have achieved impressive limits of detection in the femtomolar range over time scales of seconds to minutes.[8] Using NMEs as electrochemical biosensors enhances sensitivity by promoting efficient hybridization, and by increasing the cross section of interaction with analyte molecules. Specifically, improved radial diffusion leads to increased mass transport of analyte molecules to the electrode surface.

The present work began as an effort to eliminate costly lithographic steps previously employed in the precise definition of apertures from which NMEs are grown. Our premise was that reducing the complexity of manufacture could help further the goal enabling cost-effective POC applications, even for low-resource settings. Important related advances in this area include the recent achievement of nanostructured probe anchors based on DNA assembly,[9] thermal wrinkling of electrode substrates,[10] in situ formation of hierarchical structures,[11] and in situ growth of an array of nanostructures.[8a,12]

Our approach to NME placement and manufacture described herein was based on soft lithography techniques. Soft lithography utilizes a stamp to transfer a pattern of molecules to metal surfaces. It has been previously implemented for different applications ranging from selective etching of metals[13] to transferring a pattern of biomolecules to a substrate.[14] Here, we developed an image-reversal soft lithography (IRSL) technique that replaces high-resolution photolithographic steps previously required in the microelectrode fabrication process. We show that sufficiently controlled bottom-up nanostructured electrodes can be fabricated when the top-down definition is provided via a coarse stamping technique.

Remarkably, we found in the course of our fabrication-related studies that not only equivalent—but enhanced—performance was achieved in certain assays when IRSL-defined electrodes were employed. Specifically, we found that a newly reported blocking assay achieves superior performance compared to the reference case when concave NMEs defined by IRSL were used. The recessed growth geometry of these electrodes improved signal-to-background ratios when challenged with a specific protein analyte.

We begin by discussing the IRSL technique we developed in the present work. A poly(dimethylsiloxane) (PDMS) stamp is made by replica molding using a silicon master, enabling fabrication of a pattern of apertures on PDMS (**Figure 1**A). The stamp is used to transfer a self-assembled monolayer (SAM) of hexadecanethiol onto a gold substrate only in areas in which full contact is achieved, i.e., everywhere but in the intended apertures (Figure 1 B,C,D). We then dispense molten alkane onto the substrate and notice that the thiol layer repels the liquid alkane: as a result, the alkane is retained as droplets and is present only in the areas corresponding to the stamped apertures (Figure 1E). By spin-coating a resist layer on to the substrate containing solid alkane droplets and then melting the

T. S. Safaei, Prof. E. H. Sargent
Department of Electrical and Computer Engineering
Faculty of Applied Science and Engineering
University of Toronto
10 King's College Road, Toronto, ON M5S 3G4, Canada
E-mail: ted.sargent@utoronto.ca
Dr. J. Das, Dr. S. S. Mahshid, Prof. S. O. Kelley
Department of Pharmaceutical Science
Leslie Dan Faculty of Pharmacy
University of Toronto
144 College Street, Toronto, ON M5S 3M2, Canada
E-mail: shana.kelley@utoronto.ca
P. M. Aldridge, Prof. S. O. Kelley
Institute for Biomaterials and Biomedical Engineering
University of Toronto
164 College Street, Toronto, ON M5S 3G9, Canada
Prof. S. O. Kelley
Department of Biochemistry
Faculty of Medicine
University of Toronto
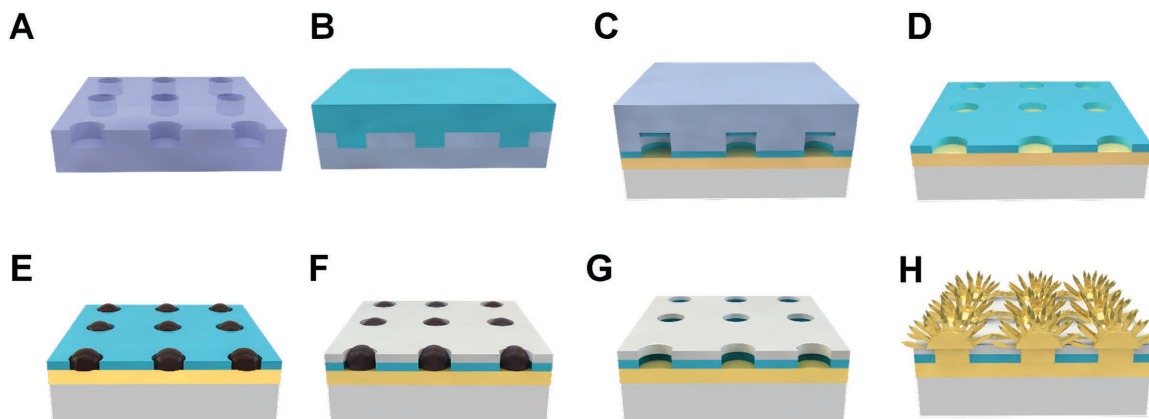1 King's College Circle, Toronto, ON M5S 1A8, Canada

Figure 1. Schematic presentation of fabrication steps of NMEs using IRSL technique. A) A patterned PDMS stamp is made by replica molding. B) The stamp is covered with a thiol layer (light blue). C) After drying, SAM of thiol is formed all over the stamp but not on the holes. D) Upon bringing the stamp into contact with the substrate, a patterned thiol SAM is transferred on to the gold layer on glass. E) Molten alkane (brown) are only retained as droplets on bare gold regions. F) Subsequently SU-8 resist (gray) is spin coated on the substrate, which now has solidified alkane droplets. G) Alkane droplets are melted again to open the apertures in the SU8 layer. H) Ultimately, everywhere else being passivated by the resist, NMEs are electroplated on the exposed regions of gold.

alkane, we thereby form apertures in the resist (Figure 1F,G). Electrochemical deposition of gold occurs therefore only in the openings, while all other areas of the chip remain insulated and passivated (Figure 1E).

Using the IRSL technique, we fabricated apertures as small as 20 μm in diameter (**Figure 2**). The thickness of the resist layer was controlled to be 50 μm. It is difficult to open small apertures reproducibly using thicker resist layers, as they may cover the solid alkane droplets and fail to produce opened apertures upon melting the droplets. Thinner resist layers fail to provide consistently complete passivation, and even small residues of undesired leftover alkane can cause holes in the
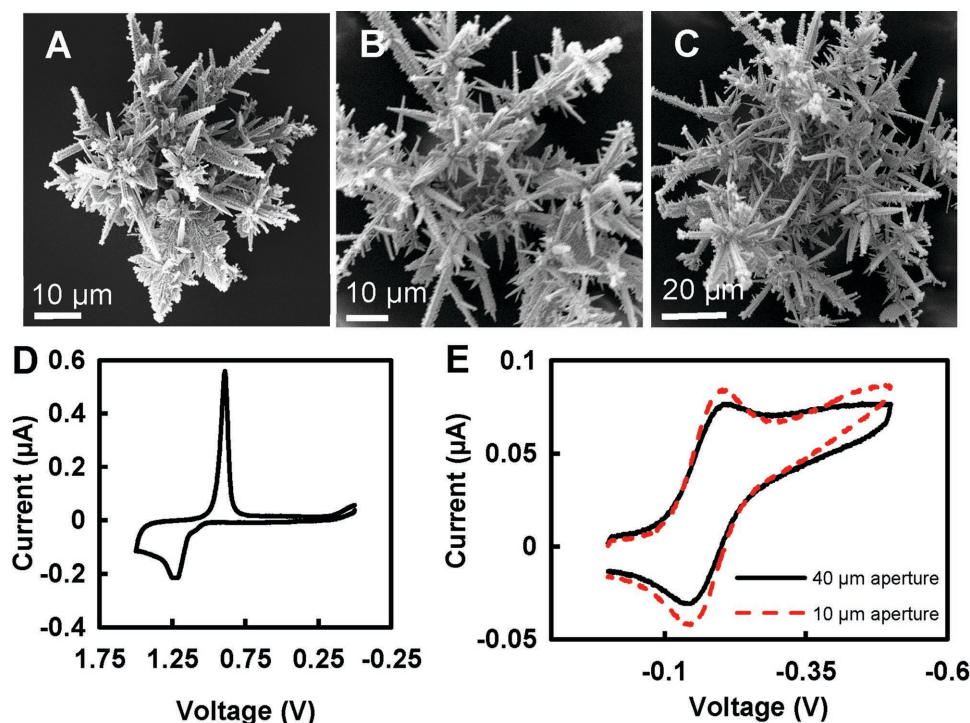

Figure 2. Optical and electrochemical characterization of NMEs. SEM images of NMEs grown using A) photolithography on 10 μm aperture and by stamping technique on B) 20 μm and C) 40 μm apertures. The images exhibit recessed growth area in the central region of NMEs made in larger apertures, resulting in less compact positioning of nanostructures. D) Acid scan of NMEs in 50×10^{-3} M H_2SO_4, demonstrate absence of any impurity. E) Cyclic voltammetry scans in 1×10^{-3} M hexamineruthenium (III) chloride demonstrate electrochemical detection of redox species using NMEs with similar active surface area made on 10 μm and 40 μm apertures. The results prove that the NMEs with recessed growth areas do not exhibit significant increase in the background signals.

www.MaterialsViews.com

ADVANCED
HEALTHCARE
MATERIALS
www.advhealthmat.de

COMMUNICATION

resist layer. Although small apertures can be made successfully using this technique, similar to conventional photolithography, fabrication yield decreases when sizes decrease below 20 μm. Above this diameter, the growth mechanism changes such that NMEs are mainly formed on the apertures edge while the central region exhibits recessed growth. This behavior is attributed to fast depletion of plating species in the center of the aperture, and this becomes more dramatic still as the NME's growth continues.[15] The morphology of NMEs made in large apertures is consequently different from that of smaller holes (Figure 2A–C). The NMEs deposited in the smaller apertures exhibit a much more compact configuration of nanostructures especially in the central regions of electrodes.[16]

We posited that, in light of this new NME architecture, the outer regions of the NMEs would benefit from more efficient mass transport through convergent diffusion of electrochemically active species. On this basis, we expect the edge of NMEs to be more active in electrochemical current generation and collection. The NMEs made in the larger apertures, on the other hand, exhibit a less compact morphology due to the recessed central regions. Therefore, we hypothesized that higher current densities can be generated with these types of NMEs, since their nanostructures are more accessible and their morphology can result in more efficient mass transport regimes.

Cyclic voltammetry (CV) of typical NMEs made using IRSL was carried out in mild sulfuric acid solution. As displayed in Figure 2D, gold reduction and oxidation occurs at the expected potentials (0.5 and 1.2 V, respectively), while no additional peak is observed, confirming the compositional metallic purity of the electroplated NMEs. Moreover, CV measurements in 1×10^{-3} M hexamineruthenium (III) chloride demonstrate the occurrence of redox reactions with no significant increase in the background signal obtained from the NME with recessed growth area (Figure 2E).

The results of 3D self-consistent finite-element numerical simulations (COMSOL Multiphysics) modeling reaction kinetics for NMEs grown in small versus large templated holes (**Figure 3**) provide quantitative confirmation of the above hypothesis. Concentration profiles of $[Ru(NH_3)_6]^{3+}$ ions show that the NMEs exhibiting recessed growth are more accessible, as they provide larger cross sections of interaction with the portion of solution that has $[Ru(NH_3)_6]^{3+}$ concentration higher than 0.1×10^{-3} M (larger red areas at close proximity to the electrodes at the steady state).

Additionally, the simulations reveal that the concentration of a redox reporter, $[Ru(NH_3)_6]^{3+}$, drops rapidly near the planar central region of electrodes. This behavior suggests that electrochemically grown electrocatalytic biosensors will be substantially insensitive to modest variations in aperture size that arise in coarse patterning, and can explain why they do not generate higher background in electrochemical scans.

The fast depletion of electroactive species in the flat regions is a result of the NMEs' constrained geometry. In previous efforts, flat microelectrodes having large areas have been expected to exhibit a high background current and consequently a low sensitivity, as their performance is negatively affected by
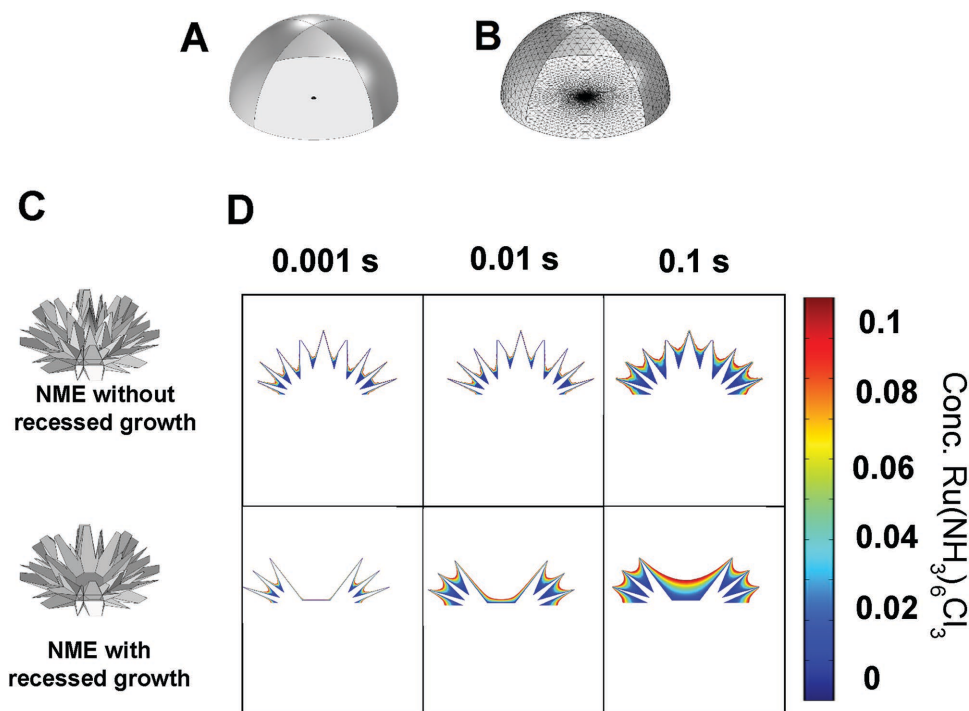

Figure 3. Simulation of reaction kinetics of NMEs with and without recessed growth. A) Geometrical configuration of 3D COMSOL simulations. NMEs were bounded by an external hemisphere ($r = 1000$ μm) held at a constant concentration of 1.0×10^{-3} M. B) Mesh for simulations. C) 3D analog of NMEs used for simulations. D) Time-varying simulation results. Concentration, c, had an initial value of 1.0×10^{-3} M at $t = 0$ s. Contours show solvent concentration for regions having 0 M $< c < 0.1 \times 10^{-3}$ M. The simulations show that NMEs with recessed growth are more accessible to the volume of solution with Ru concentrations above 0.1×10^{-3} M. Also, the fast depletion in the flat regions of electrodes suggests that those areas are not active in generation of redox signals.
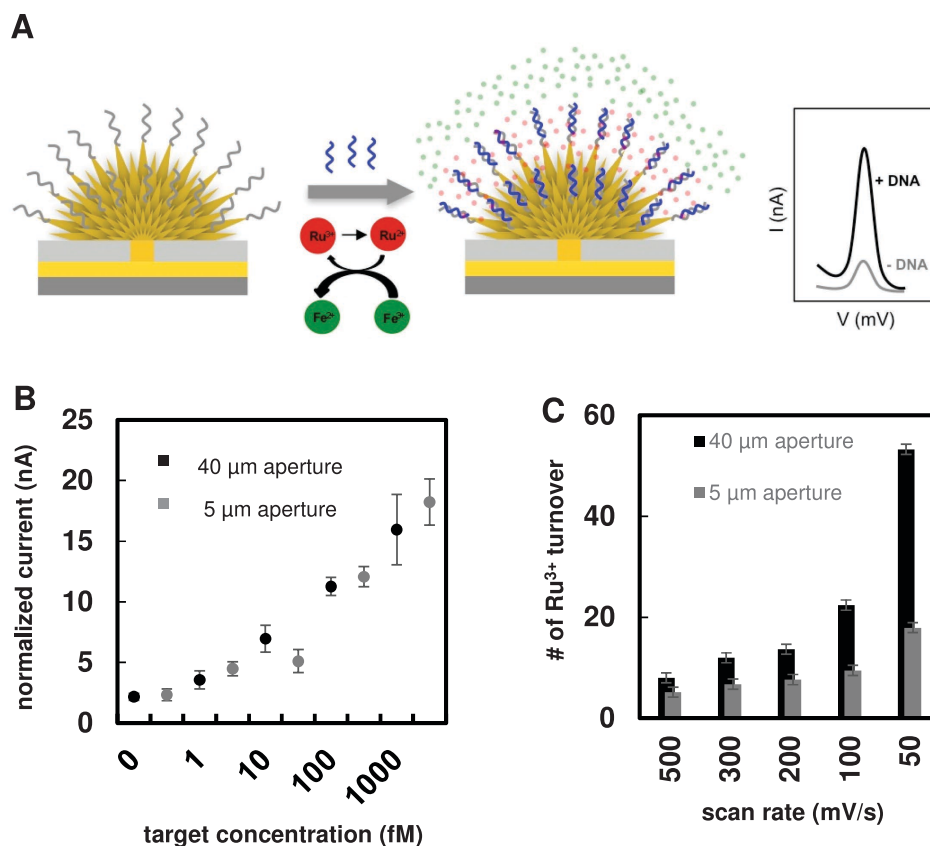
COMMUNICATION

Figure 4. Biosensor performance validation. A) Schematic of a Ru–Fe electrocatalytic system, showing increased attraction of Ru^{3+} (red circles) to NMEs upon target (blue strands) hybridization with PNA probe (gray strands) that results in an increase in Ru reduction signal. The signal gain indicates the presence of specific target molecules. Fe molecules (green circles) readily reoxidize Ru^{2+} ions, so they will be available for another redox cycle, which amplifies the signal gain and enhances the system's sensitivity. B) A specific nucleic acid sequence was successfully detected in the femtomolar range with Ru–Fe electrocatalytic system using NMEs fabricated by IRSL. The obtained signal from detection of a non-complementary (NC) sequence demonstrates the specificity of the technique. C) Higher number of turnover of Ru ions is obtained with NME made on larger apertures.

inadequate mass transport of ions. In these studies, we show that only the nanostructured regions of electrodes—those that support radial diffusion—are active areas for redox reactions. The central flat regions deplete rapidly of active species and do not significantly contribute to electrochemical signals. As a result, the overall mass transport towards NMEs with recessed growth is more efficient compared not only to flat microelectrodes, but also to NMEs lacking recessed growth regions.

Further evaluation of the NMEs' performance in the detection of biological samples was carried out based on electrochemical detection of specific nucleic acid sequences using the electrocatalytic Ru–Fe system.[8b,17] The protruding structures of electroplated gold provide anchors for effective binding of PNA probes to the electrode using thiolated linkers. Negatively charged phosphate present in the backbone of target nucleic acids attracts positively charged redox ions such as, in the present case, $[Ru(NH_3)_6]^{3+}$. Upon target and probe hybridization, the $[Ru(NH_3)_6]^{3+}$ ions are attracted to the electrode surfaces and thereby reduced given their proximity to the electrodes. The amount of attracted $[Ru(NH_3)_6]^{3+}$ ions is directly controlled by the number of phosphate ions. As a result, a larger reduction current is generated in the presence of a higher concentration of target nucleic acids. Moreover, in the Ru–Fe systems,

Ru reduction turnover and signal gain are amplified due to simultaneous reduction of $[Fe(CN)_6]^{3+}$, which reoxidizes Ru^{2+} species and makes them available for additional redox cycles (**Figure 4A**).

Using the electrocatalytic system and an electrode made via the IRSL method having target aperture diameter of 40 µm, we demonstrated successful detection of synthetic oligonucleotides with clinically relevant levels of sensitivity and specificity. An impressively low limit of detection is achieved as a result of the coupling of NMEs features with the reporter system's characteristics. Specifically, a statistically significant difference is seen between 1×10^{-15} M concentration of target-containing solution compared to the non-complementary reference case (Figure 4B). Moreover, the same amplitude of electrical current is achieved by lithographically defined NMEs made in 5 µm apertures when fully three times higher analyte concentrations are provided. The background signals collected in the presence of non-complementary targets are at the same low level in each case.

The enhanced performance of the coarsely templated NMEs is attributed to their higher accessibility. This characteristic can be further demonstrated by studying the number of catalytic cycles of Ru^{3+} regeneration. A higher number of Ru^{3+} turnovers
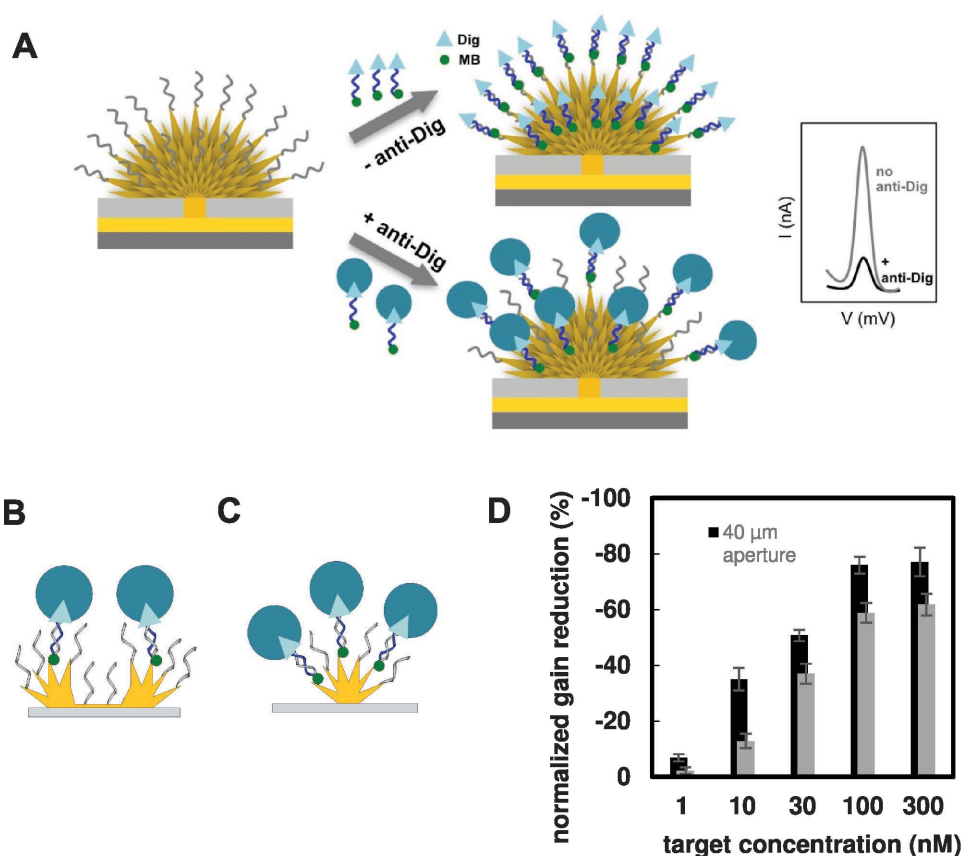
Figure 5. Schematic representation of an electrochemical steric hindrance hybridization assay and its performance on different types of NMEs. A) Capturing DNA probes (gray strands) are immobilized on the surface of electrode that are complementary to secondary carrier DNA strand (blue strands). The carrier strand is dual labeled with a small recognition element (digoxigenin) and a signaling redox tag of methylene blue [green circles]. The recognition element is specific to the target molecule (anti-digoxigenin antibody), therefore in presence of large target proteins, steric hindrance does not allow carrier strands hybridization to the probes greater than a certain degree. As a result the signal generated in presence of anti-digoxigenin molecules are less than the reference signals obtained with no target molecule. B) NMEs with recessed growth area provide a constraining geometry resulting in blocking of the probes trapped in the central regions, thus producing larger gain reductions. C) Whereas NMEs without recessed growth have higher ability to accommodate large molecules on their surface. D) Gain reduction percentage is higher for the NMEs made on larger apertures, proving their enhanced blocking effects.

achieved from NMEs made on larger apertures (Figure 4C) is indicative of the more efficient mass transport of electroactive species to the electrodes' surfaces.

We further hypothesized that the concave geometry of the new NMEs based on recessed growth could make these electrodes favorable for improved implementation of blocking assays. We focused in on one such recently reported assay, the electrochemical steric hindrance hybridization assay (eSHHA).[18] In eSHHA, the reporter molecules (in this case methylene blue) are bound to one end of secondary oligonucleotides. These molecules generate electrochemical signals when they are placed on the electrodes' surfaces via hybridization of their carrier oligonucleotides with probe strands. The target molecules are specifically attached to the carrier oligonucleotides using an appropriate recognition element, one that previously was bound to the other end of the secondary oligonucleotides. The large size of the target molecules provides steric hindrance, and this prevents the successful hybridization of secondary oligonucleotides containing methylene blue with the probes. As a result, signals generated in presence of target

proteins are lower compared to the reference current that is collected in the absence of the target molecule. The key figure of merit, the relative gain reduction $\left(\frac{I_{\text{target}} - I_{\text{reference}}}{I_{\text{reference}}} \right)$, is proportional to the concentration of target proteins (**Figure 5**A). Here we used digoxigenin as the recognition element and antidigoxigenin antibodies as the target molecules.

We employed eSHHA in the detection of proteins and found that NMEs made in larger apertures exhibited higher values of gain reduction compared to those ones made in small, conventional lithographical NME apertures. The constraining geometry of NMEs with recessed growth (Figure 5B,C) enhances blocking effects (Figure 5D), with the distinctive morphology of such NMEs impeding the diffusion of large molecules to the central regions during the relatively short measurement times.

In summary, we demonstrate that fabrication of NMEs on coarse templates. This allows cost-effective photolithography-free bioanalytical integrated circuit fabrication. Additionally, using coarser templates allows formation of structures

exhibiting a new geometry that enhances performance in both electrocatalytic and blocking assays. We further demonstrate that it is possible to achieve very low limits of detection and clinically relevant levels of sensitivity in electrochemical biosensing while employing these coarse fabrication techniques. The image reversal soft lithography method was proposed as a simple alternative for photolithographic fabrication of these NMEs. Future directions include demonstration of alignment techniques for multilevel IRSL, as well as even more cost-effective fabrication employing lower-cost polymers than SU-8.

More broadly, enhanced electrochemical performance of electrodes made on coarser templates open new avenues to biosensor integrated circuits' facile fabrication employing cost-effective methods, including inkjet printing. Emerging techniques of biosensor fabrication will thus enable automated and high-throughput fabrication of potentially more sensitive electrochemical biosensors and contribute to increasing the range of economically feasible POC devices.

Experimental Section

Photolithographic Fabrication: Glass chips were purchased form Telic (Valenica, CA). They were precoated using 5 nm Cr and 50 nm Au and a layer of AZ1600 positive photoresist. The substrates were selectively exposed using 900 W UV for 12 s and developed in MF312 for 40 s. The patterning of electrodes as realized by wet etching of Au and Cr in the unprotected areas. Subsequently, negative photoresist (SU-8 2002) was spin-cast on the chips at 4500 rpm, for 40 s, exposed for 12 s and developed for 1 min, to form the apertures having 10 μm diameter.

Image Reversal Soft Lithography: Using SU-8 3050, 70 μm tall posts of various diameters was fabricated on silicon (spin-coated at 1500 rpm for 40 s, exposed for 23 s and developed in SU-8 developer for 8 min). The silicon wafer served as the master for molding PDMS (Dow Chemical, MI) to fabricate a stamp to define the holes. The stamp was then dipped in 3×10^{-3} M 1-hexadecanethiol (Sigma, MO) solution in IPA and allowed to dry completely under a light stream of nitrogen gas.

SAM of thiol was formed on the substrate upon full contact with the stamp. Molten alkane (paraffin wax, Sigma, MO) was poured on the substrate, which was kept heated at 95 °C. The thiol layer repelled the alkane, permitting it to be wicked off of the chip. Only small droplets of alkane remained, and only in the the areas corresponding to the stamp holes. The substrate was then cooled and spin-coated with SU-8 3010 at 1500 rpm for 40 s. When the chip was then heated (15 s at 95 °C), the resist layer solidified while alkane droplets melted and could be washed away using IPA and water, opening up well-defined apertures in the resist.

Fabrication of the Nanostructured Microelectrodes: Chips were cleaned using isopropyl alcohol and DI water, and dried using a flow of nitrogen. Electrodeposition was carried out at room temperature. Apertures exposing gold formed the working electrode; these were contacted using exposed bond pads. The Au sensor was made using a deposition solution containing 50×10^{-3} M solution of $HAuCl_4$ and 0.5 M HCl using DC potential amperometry at 0 mV for 100 s. Ensuingly, the Au sensors were coated with a thin layer of Pd to form nanostructures by replating in a solution containing 5×10^{-3} M $PdCl_2$ and 0.5 M $HClO_4$ at −250 mV for 10 s.

PNA Probe Design for Ru–Fe Assay: PNA probe (Cys-AEEA-5′-TTG TGG TAC TGC CTG ATA GGG-3′) was obtained from PNA Bio Inc., Canada. Synthetic complementary target (5′-CCC TAT CAG GCA GTA CAA CAA-3′) and non-complementary target (5′-TAG CTA CAG AGA AAT TC-3′) were obtained from ACGT, Canada. Probe and DNA sequences were quantified by measuring absorbance at 260 nm using a NanoDrop.

Functionalization and Hybridization of Electrodes for Ru–Fe Assay: Aqueous solution containing 2×10^{-6} M of PNA probe was mixed with 20×10^{-6} M of aqueous TCEP. The mixture was left for 1 h to cleave disulphide bonds. After 18×10^{-6} M of 6-mercaptohexanol (MCH) were mixed into this solution, 50 μL of the resultant solution was pipetted onto the chips and incubated overnight in a dark humidity chamber at room temperature to provide probe immobilization. The integrated circuits were then washed twice for 5 min using 1× PBS at room temperature. After washing, the chips were challenged with different concentrations of targets, in each case for 30 min and at room temperature. After hybridization, the chips were washed twice for 5 min with 1× PBS at room temperature and the electrochemical scans were acquired.

Electrochemical Measurements for Ru–Fe Assay: All electrochemical measurements were performed using the BASi EC Epsilon potentiostat in the standard three-electrode configuration with Ag/AgCl reference and Pt wire counter electrodes. To study the effective surface area of the NMEs, CV scans were recorded in 50×10^{-3} M H_2SO_4 solution in the potential window of 0 to 1.5 V with 100 mV s^{-1} scan rate.

Ru and Fe scans were carried out in 1×10^{-3} M $Ru(NH_3)Cl_3$ and 2×10^{-3} M $K_4Fe(CN)_6$ in 1× PBS solution between −0.5 to 0 V and 0 to 0.5 V, respectively. Ru solution was purged with nitrogen for 15 min before the tests to remove the oxygen content.

To measure the amount of hybridized nucleic acid, electrochemical signals were measured in 0.1× PBS with 10×10^{-6} M $[Ru(NH_3)_6]Cl_3$ and 4×10^{-3} M $K_3[Fe(CN)_6]$. DPV signals were obtained with a potential step of 5 mV, pulse amplitude of 50 mV, pulse width of 50 ms, and a pulse period of 100 ms. Signal changes that corresponded to target hybridization were calculated based on background-subtracted currents: $\Delta I = (I_{after} - I_{before})$ (where I_{after} = current after target hybridization and I_{before} = current before target hybridization, i.e., current with only probe). All current values obtained from electrodes made on smaller apertures were rescaled to normalize to the surface of area of electrodes. This factor is the ratio of geometric surface area of the electrodes made in larger aperture to the geometric surface area of electrodes made in smaller apertures. The error bars represent the standard error of measurements.

Ru Turnover Experiment: 50 μL of PBS solution containing 1×10^{-6} M of thiolated ssDNA (5′-CCG CGA GAC TGC TAG C-3′), obtained from Integrated DNA Technologies (IDT), USA), 20×10^{-6} M of TCEP, and 50×10^{-3} M of $MgCl_2$ was pipetted on to the chips and incubated overnight in a dark humidity chamber at room temperature for DNA immobilization. The chips were then washed twice for 5 min with 1× PBS at room temperature.

To obtain turnover numbers, CV was obtained at ssDNA-modified NME at different scan rates in 0.1× PBS solutions containing only 10×10^{-6} M $[Ru(NH_3)_6]^{3+}$ and then solutions containing 10×10^{-6} M $[Ru(NH3)6]^{3+}$ and 4×10^{-3} M $[Fe(CN)_6]^{3-}$. A ratio of catalyzed to uncatalyzed background subtracted cathodic peak currents was representing turnover.

Target Solution Preparation and Probe Design for eSHHA: Polyclonal anti-digoxigenin antibody (Roche Diagnostics, Indianapolis, IN) was dissolved in 1× PBS (pH 7). The solution was then used to prepare different concentrations of target solutions. Probe DNA strands (5′-HS-(CH2)6-AAGG AAA GGG AAG AAG) and signaling/carrier DNA strands (5′-Digoxigenin-CTT CTT CCC TTT CCTT-MB(Methylene Blue)) were obtained from Biosearch Technologies Inc., Novato, CA.

Functionalization of Electrodes for eSHHA: DNA probes (0.1×10^{-3} M) were activated by 1×10^{-6} M TCEP solution for 1 h to remove disulfide bonds. Further the probe solution was diluted in PBS to get final probe concentration of 100×10^{-9} M. Electrodes were then incubated in 50 μL of probe solution overnight. Subsequently, the chips were incubated in 3×10^{-3} M MCH in buffer for 3 h to passivate the remaining electrodes area. Electrodes were thoroughly washed with PBS prior to testing.

Electrochemical Measurements for eSHHA: The EmStatMUX potentiostat multiplexer (Palmsens Instruments, Netherland) was used for electrochemical measurements of eSHHA with standard three-electrode configuration against Ag/AgCl reference electrode. The square wave voltammetry technique was used to obtain the electrochemical signals. The potential was swept from 0.2 to −0.4 V in increments of 0.001 V, with a pulse amplitude of 50 mV at frequency of 60 Hz. All measurements were taken immediately following addition of target solution to 100×10^{-9} M of carrier strands without any prior incubation

www.MaterialsViews.com

ADVANCED
HEALTHCARE
MATERIALS

www.advhealthmat.de

COMMUNICATION

period. As in the case of Ru–Fe data, results were normalized to the geometric area of electrodes and the error bars represent the standard error values of each measurement.

COMSOL Simulations: 3D, time-dependent simulations of standard and fabless NMEs were carried out using the electroanalysis module of COMSOL Multiphysics. Electrode geometries were designed to represent the morphologies of the respective electrode types. An initial solution concentration of 1×10^{-3} M Ru(NH3)$_6$Cl$_3$, diffusion constant of 2×10^{-5} cm^2 s^{-1}, and applied potential of -0.12 V were used as parameters in all simulations. A hemispherical external boundary was situated far from the electrodes (1000 μm) in order to approximate the unbounded case over the time period studied; a constant concentration of 1×10^{-3} M was imposed on the external boundary. In order to increase the resolution of the concentration profile at close proximity of the electrodes, 0.1×10^{-3} M was set as the cutoff.

Electron Microscopy: Scanning electron images of NMEs were taken by FEI-Quanta 250 FEG at 15 KV accelerating voltage.

Acknowledgements

[1] a) D. R. Walt, *Science* **2005**, *308*, 5719; b) S. O. Kelley, C. A. Mirkin, D. R. Walt, R. F. Ismagilov, M. Toner, E. H. Sargent, *Nat. Nanotechnol.* **2014**, *9*, 12.

[2] a) J. M. Nam, C. S. Thaxton, C. A. Mirkin, *Science* **2003**, *301*, 5641; b) A. V. Kabashin, P. Evans, S. Pastkovsky, W. Hendren, G. A. Wurtz, R. Atkinson, R. Pollard, V. A. Podolskiy, A. V. Zayats, *Nat. Mater.* **2009**, *8*, 11; c) G. J. Nusz, S. M. Marinakos, A. C. Curry, A. Dahlin, F. Höök, A. Wax, A. Chilkoti, *Anal. Chem.* **2008**, *80*, 4; d) O. Scheler, J. T. Kindt, A. J. Qavi, L. Kaplinski, B. Glynn, T. Barry, A. Kurg, R. C. Bailey, *Biosens. Bioelectron.* **2012**, *36*, 1.

[3] a) A. Gao, N. Lu, Y. Wang, P. Dai, T. Li, X. Gao, Y. Wang, C. Fan, *Nano Lett.* **2012**, *12*, 10; b) S. Sorgenfrei, C. Y. Chiu, R. L. Gonzalez, Y. J. Yu, P. Kim, C. Nuckolls, K. L. Shepard, *Nat. Nanotechnol.* **2011**, *6*, 2; d) Y. L. Bunimovich, Y. S. Shin, W. Yeo, M. Amori, G. Kwong, J. R. Heath, *J. Am. Chem. Soc.* **2006**, *128*, 50; e) X. Duan, C. M. Lieber, *Nano Res.* **2015**, *8*, 1.

[4] a) P. T. Burg, M. Godin, S. M. Knudsen, W. Shen, G. Carlson, J. S. Foster, K. Babcock, S. R. Manalis, *Nature* **2007**, *446*, 7139; b) A. K. Naik, M. S. Hanay, W. K. Hiebert, X. L. Feng, M. L. Roukes, *Nat. Nanotechnol.* **2009**, *4*, 7; c) M. S. Hanay, S. Kelber, A. K. Naik, D. Chi, S. Hentz, E. C. Bullard, E. Colinet, L. Duraffourg, M. L. Roukes, *Nat. Nanotechnol.* **2012**, *7*, 9.

[5] a) E. Vasilyeva, B. Lam, Z. Fang, M. D. Minden, E. H. Sargent, S. O. Kelley, *Angew. Chem., Int. Ed.* **2011**, *50*, 18; b) R. Malhotra, V. Patel, J. P. Vaqué, J. S. Gutkind, J. F. Rusling, *Anal. Chem.* **2010**, *82*, 8; c) Y. Wan, Y. Zhou, M. Poudineh, T. Saberi Safaei, R. M. Mohamadi, E. H. Sargent, S. O. Kelley, *Angew. Chem., Int. Ed.* **2014**, *53*, 48; d) T. Saberi Safaei, R. M. Mohamadi, E. H. Sargent, S. O. Kelley, *ACS Appl. Mater. Interfaces* **2015**, *7*, 26.

[6] a) J. Wang, *Biosens. Bioelectron.* **2006**, *21*, 10; b) C. Fan, K. W. Plaxco, A. J. Heeger, *Proc. Natl. Acad. Sci.* **2003**, *100*, 16; c) J. C. Liao, M. Mastali, V. Gau, M. A. Suchard, A. K. Møller, D. A. Bruckner, J. T. Babbitt, Y. Li, J. Gornbein, E. M. Landaw, E. R. B. McCabe, B. M. Churchill, D. A. Haake, *J. Clin. Microbiol.* **2006**, *44*, 2; d) J. Wang, G. Liu, A. Merkoçi, *J. Am. Chem. Soc.* **2003**, *125*, 11.

[7] a) P. E. Sheehan, L. J. Whitman, *Nano Lett.* **2005**, *5*, 4; b) T. M. Squires, R. J. Messinger, S. R. Manalis, *Nat. Biotechnol.* **2008**, *26*, 4.

[8] a) E. Stern, J. F. Klemic, D. A. Routenberg, P. N. Wyrembak, D. B. Turner-Evans, A. D. Hamilton, D. A. LaVan, T. M. Fahmy, M. A. Reed, *Nature* **2007**, *445*, 7127; b) L. Soleymani, Z. Fang, B. Lam, X. Bin, E. Vasilyeva, A. J. Ross, E. H. Sargent, S. O. Kelley, *ACS Nano* **2011**, *5*, 4; c) A. T. Sage, J. D. Besant, B. Lam, E. H. Sargent, S. O. Kelley, *Acc. Chem. Res.* **2014**, *47*, 8; d) Z. Fang, L. Soleymani, G. Pampalakis, M. Yoshimoto, J. A. Squire, E. H. Sargent, *ACS Nano* **2009**, *3*, 3207.

[9] a) M. Lin, J. Wang, G. Zhou, J. Wang, N. Wu, J. Lu, J. Gao, X. Chen, J. Shi, X. Zuo, C. Fan, *Angew. Chem., Int. Ed.* **2015**, *54*, 7; b) H. Pei, X. Zuo, D. Pan, J. Shi, Q. Huang, C. Fan, *NPG Asia Mater.* **2013**, *5*, 6.

[10] a) C. M. Gabardo, Y. Zhu, L. Soleymani, J. M. Moran-Mirabal, *Adv. Funct. Mater.* **2013**, *23*, 24; b) S. M. Woo, C. M. Gabardo, L. Soleymani, *Anal. Chem.* **2014**, *86*, 24.

[11] a) X. Lu, H. Zhang, Y. Ni, Q. Zhang, J. Chen, *Biosens. Bioelectron.* **2008**, *24*, 1; b) Z. Wen, S. Ci, J. Li, *J. Phys. Chem. C* **2009**, *113*, 31.

[12] Z. Fang, S. O. Kelley, *Anal. Chem.* **2008**, *81*, 2.

[13] a) J. L. Wilbur, A. Kumar, E. Kim, G. M. Whitesides, *Adv. Mater.* **1994**, *6*, 7; b) A. P. Quist, E. Pavlovic, S. Oscarsson, *Anal. Bioanal. Chem.* **2005**, *381*, 3.

[14] a) E. Delamarche, *Protein Science Encyclopedia*, Wiley, Hoboken, NJ **2000**; b) C. D. James, R. C. Davis, L. Kam, H. G. Craighead, M. Isaacson, J. N. Turner, W. Shain, *Langmuir* **1998**, *14*, 4.

[15] B. Lam, R. D. Holmes, J. Das, M. Poudineh, A. Sage, E. H. Sargent, S. O. Kelley, *Lab Chip* **2013**, *13*, 13.

[16] Y. Zhou, Y. Wan, A. T. Sage, M. Poudineh, S. O. Kelley, *Langmuir* **2014**, *30*, 47.

[17] a) L. Soleymani, Z. Fang, E. H. Sargent, S. O. Kelley, *Nat. Nanotechnol.* **2009**, *4*, 12; b) X. Bin, E. H. Sargent, S. O. Kelley, *Anal. Chem.* **2010**, *82*, 14.

[18] S. S. Mahshid, S. Camiré, F. Ricci, A. Vallée-Bélisle, *J. Am. Chem. Soc.* **2015**, *137*, 50 .